

# Vapor-Transport Synthesis and Annealing Study of $Zn_xMg_{1-x}O$ Nanowire Arrays for Selective, Solar-Blind UV-C Detection

Ebraheem Ali Azhar,<sup>\*,†</sup> Jignesh Vanjaria,<sup>‡</sup> Seungho Ahn,<sup>†</sup> Thomas Fou,<sup>†</sup> Sandwip K. Dey,<sup>‡</sup> Tom Salagaj,<sup>§</sup> Nick Sbrockey,<sup>§</sup> Gary S. Tompa,<sup>§</sup> and Hongbin Yu<sup>\*,†</sup>

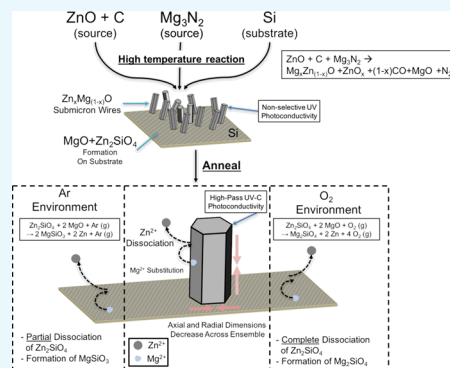
<sup>†</sup>School of Electrical, Computer and Energy Engineering, Arizona State University, 650 E Tyler Mall, Tempe, Arizona 85281, United States

<sup>‡</sup>School for Engineering of Matter, Transport and Energy, Arizona State University, 501 E Tyler Mall, Tempe, Arizona 85287, United States

<sup>§</sup>Structured Materials Industries Inc., 201 Circle Drive North, Piscataway, New Jersey 08854, United States

## Supporting Information

**ABSTRACT:** This work uniquely reports the synthesis of  $Zn_xMg_{1-x}O$  nanowires and submicron columns by utilizing a traditional carbothermal reduction process toward forming ZnO nanowire ultraviolet detectors, while simultaneously utilizing  $Mg_3N_2$  as the source of Mg. To investigate the relationship between Mg content in the ZnO lattice and the cutoff wavelength for high spectral responsivity, the nanowires were annealed in a series of designed conditions, whereas chemical, nanostructural, and optoelectronic characteristics were compared before and after treatment. Postanneal scanning electron micrographs revealed a reduction of the average ensemble nanowire dimensions, which was correlated to the modification of ZnO lattice parameters stemming from  $Zn^{2+}$  dissociation and  $Mg^{2+}$  substitution (confirmed via Raman spectroscopy). The analysis of cathodoluminescence spectra revealed a blueshift of the peak alloy band-edge emission along with a redshift of the ZnO band-edge emission; and both were found to be strong functions of the annealing temperature. The conversion of  $Zn_2SiO_4$  to  $Mg_2SiO_4$  (in  $O_2$ ) and  $MgSiO_3$  (in Ar) was found to correspond to transformations (shifting and scaling) of high-energy luminescence peaks and was confirmed with X-ray diffraction analysis. The tunability of the cutoff photodetection wavelength was evaluated as the nanowire arrays exhibited selective absorption by retaining elevated conduction under high-energy UV-C irradiation after thermal treatment but exhibiting suppressed conductivity and a single order of magnitude reduction in both spectral responsivity ( $R_\lambda$ ) and photoconductive gain ( $G$ ) under UV-A illumination. Noise analysis revealed that the variation of detectivity ( $D^*$ ) depended on the regime of ultraviolet irradiation, and that these variations are related to thermal noise resulting from oxygen-related defects on both nanowire and substrate surfaces. These results suggest a minor design tradeoff between the noise characteristics of thermally treated ZnMgO nanowire array UV detectors and the tunability of their spectral sensitivity.



## 1. INTRODUCTION

Ultraviolet, solar-blind communication systems that exploit atmospheric scattering to propagate signals toward a nonlinear sight receiver (with ranges on the order of kilometers) have been examined extensively, yet the detectors in these receiver systems have largely been dominated by bulky and costly photomultiplier tubes.<sup>1–3</sup> Semiconductor-based deep-UV detectors have consequently become of great interest due to their potential advantages of producing low-cost, low-power-consumption, highly scalable solutions. Although ZnO nanowire (NW)-based photodetectors have been heavily investigated, this material system only exhibits a cutoff detection corresponding to the band-edge energy of ZnO in the UV-A spectrum (3.10–3.94 eV).<sup>4–6</sup> Substitutional doping of Mg with ZnO, on the other hand, has been described as a means of engineering the bandgap of a ternary  $Zn_xMg_{1-x}O$  system as

high as a 5.8 eV for solar-blind photodetectors.<sup>7–10</sup> Although Mg has been reported as a feasible dopant to ZnO (due to the similar ionic radii of  $Zn^{2+}$  and  $Mg^{2+}$ ),<sup>11,12</sup> Mg/ZnO alloy systems have also shown to phase segregate for high Mg content.<sup>13</sup> Thus, the development of reliable techniques toward synthesizing aligned ZnO nanowires, and appreciably incorporating Mg during synthesis is of great significance. Prior work investigating ZnMgO nanostructures have been reported based on deposition methods, which have ranged from: molecular beam epitaxy,<sup>14</sup> metal–organic chemical vapor deposition,<sup>15,16</sup> pulsed-laser deposition,<sup>17</sup> hydrothermal techniques,<sup>8,18</sup> radio frequency magnetron cosputtering,<sup>19</sup> and vapor-phase trans-

Received: September 13, 2017

Accepted: December 26, 2017

Published: May 4, 2018

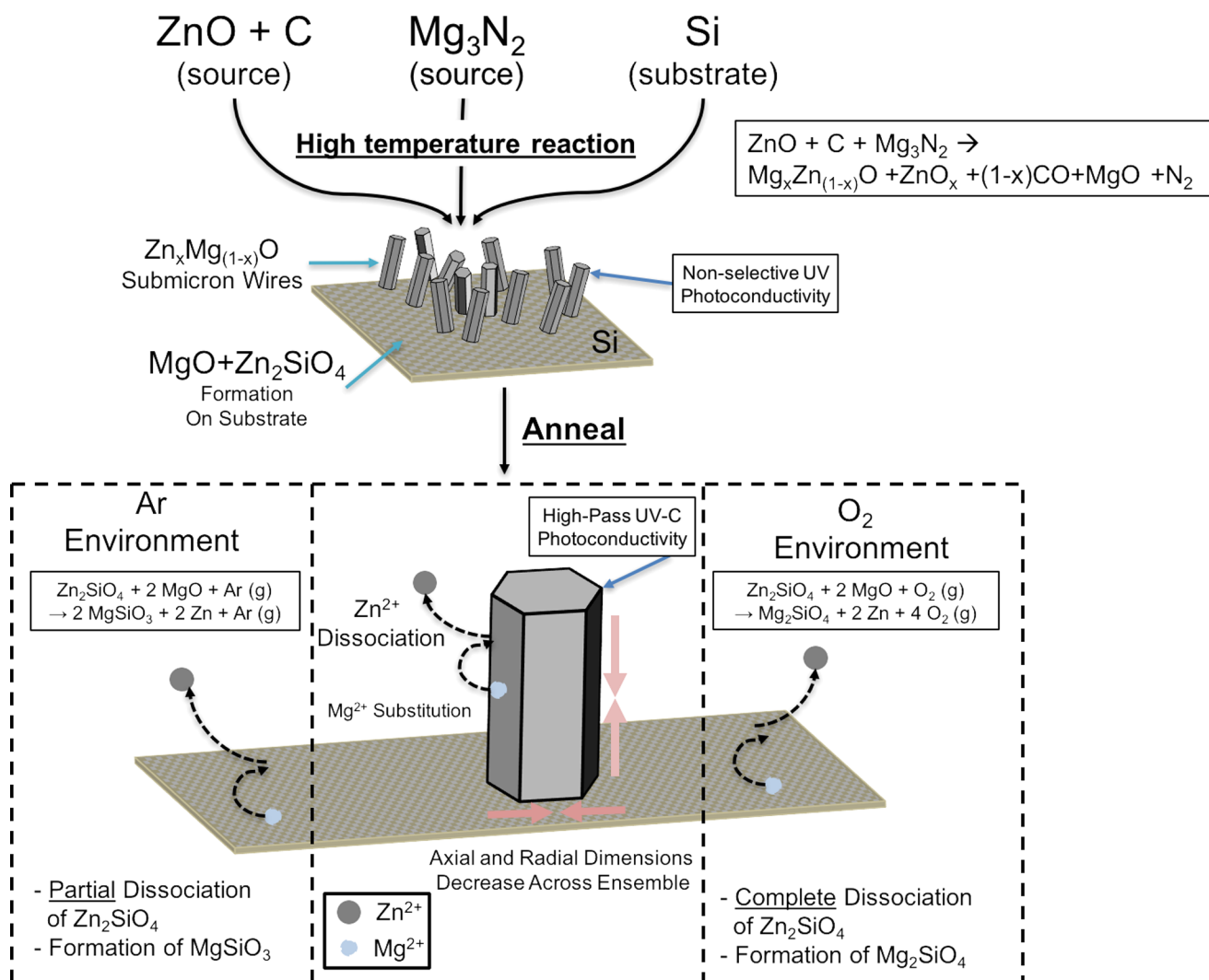


**Figure 1.** Schematic of reaction mechanisms forming ZnMgO nanowires, along with structural and chemical modifications from thermal treatment.

port.<sup>7,10,20</sup> The vapor-phase transport technique yields highly crystalline nanostructures and is a relatively straightforward synthesis route, able to encompass equilibrium formation in one step, rather than necessitating ex situ incorporation. Additionally, understanding the changes in optical and physical properties due to postgrowth thermal treatment of ZnMgO nanowires is of importance toward tuning the cutoff wavelength for solar-blind photodetectors.

In this study, ZnMgO nanowires and submicron columns were synthesized on Si via two equilibrium processes occurring simultaneously: (1) the carbothermal reduction of ZnO and (2) the incorporation of Mg from dissociated  $\text{Mg}_3\text{N}_2$ , which to the best knowledge of the authors has not been reported. Furthermore, a controlled post growth annealing study varying annealing environment and annealing temperature was conducted, demonstrating an evolution of the chemical, spectral, and optoelectronic properties of the synthesized ZnMgO nanostructures. Assessed both before and after thermal treatments, these modified characteristics were investigated via field emission scanning electron microscopy (FESEM), energy-dispersive X-ray (EDX) spectroscopy, X-ray diffraction (XRD), Raman spectroscopy, cathodoluminescence (CL), and current–voltage ( $I$ – $V$ ) behavior. The structural changes of ZnMgO nanowires manifested as modifications of the aspect

ratio, while also correlating to modified estimates of Mg incorporation due to each annealing condition. Analysis of spectral responsivity and photoconductive gain between treatment and control groups was conducted under dissimilar ultraviolet regimes to numerically compare the differences within detector performance. By exploiting the achieved controlled reaction kinetics from thermal annealing, enhanced selective filtering of high-energy UV-C absorption on the nanowire ensemble is demonstrated, accompanied by suppressed conductivity under UV-A illumination. Additionally, analysis of detector noise characteristics demonstrated that their variation from ultraviolet irradiation was linked to the increase of thermal noise from increased oxygen-related defects, presenting potential performance tradeoffs.

## 2. RESULTS AND DISCUSSION

Figure 2a shows the scanning electron micrograph (SEM) of the as-synthesized ZnMgO nanowire arrays, with a zoomed view of a single nanowire in the inset. The wires exhibited a vertical (yet regularly offset by a slight angle) growth pattern with a characteristic coarse surface texture. Energy-dispersive X-ray (EDX) spectroscopy mapping presented in Figure 2b further revealed the elemental composition of the nanowires, confirming the incorporation of Mg. As seen in Figure 2d, EDX

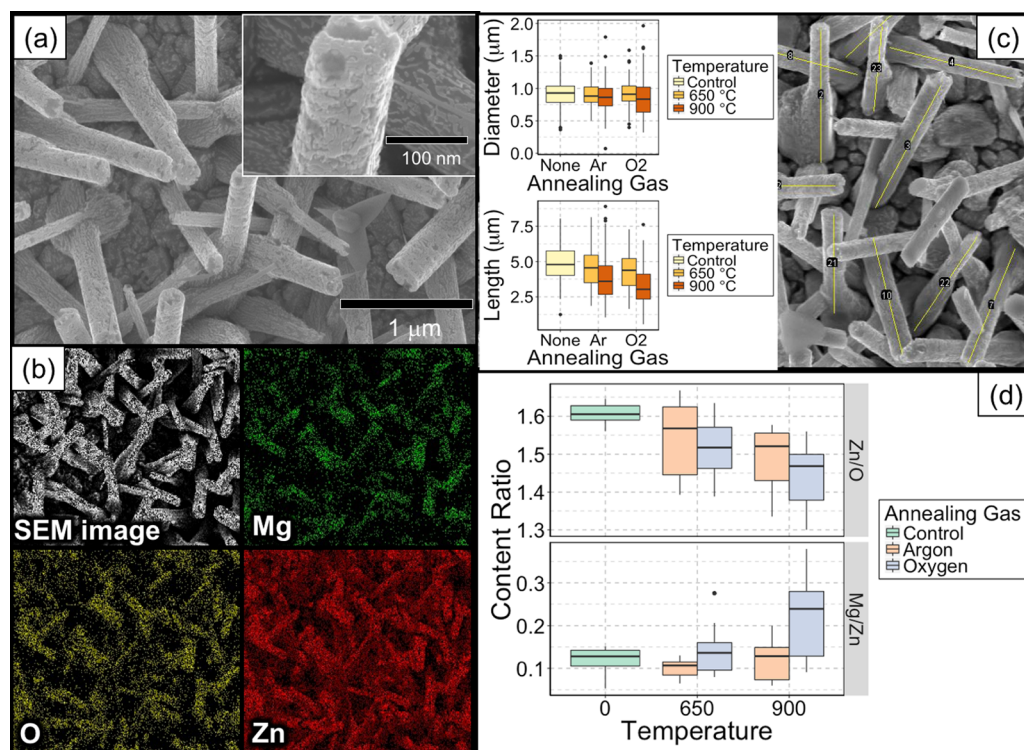


**Figure 2.** (a) SEM micrograph of ZnMgO nanowire array (inset: zoomed view of single wire). (b) EDX mapping of grown nanowires, uncovering spatial resolution of Zn, Mg, and O<sub>2</sub> constituents. (c) Left: measured size distributions (top: diameter, bottom: length) of nanowires for each anneal treatment group. Right: sample micrograph of traced nanowire lengths, post annealing. (d) Elemental atomic ratio as a function of anneal temperature and anneal gas.

quantification analysis shows that the Mg content relative to Zn extends as high as 15% upon the initial synthesis. A growth mechanism that accounts for the carbothermal reduction of ZnO with a Mg<sub>3</sub>N<sub>2</sub> source yields reaction products of Zn<sub>x</sub>Mg<sub>1-x</sub>O, ZnO, MgO, and Zn<sub>2</sub>SiO<sub>4</sub>, as illustrated in Figure 1. Upon subjecting the nanowires to each anneal condition, the average relative composition of Mg in all anneal cases widens in variance, and is most pronounced when annealed in O<sub>2</sub> at 900 °C. In this case, the median Mg content relative to Zn is found to be approximately 24%, as shown in Figure 2d. Similarly reported experiments have indicated that the alloying Mg content reaches saturation due to phase segregation, despite larger annealing temperatures.<sup>8</sup> From Figure 2c the effect of annealing on nanowire size (diameter and length) does not ostensibly appear pronounced, however an analysis of variance (ANOVA) coupled with a pairwise Tukey's range test confirms a statistically significant reduction in the distributions of both nanowire dimensions, especially for higher temperature (see Tables S1 and S2, Supporting Information). This reduction is explained by a modification of the underlying ZnO nanostructure, with Zn<sup>2+</sup> vaporizing and dissociating from the nanowire,<sup>21</sup> allowing Mg<sup>2+</sup> to occupy the vacancies and integrate within the crystal lattice. As presented in Figure 2d, this process is evidenced by a decrease of relative Zn/O content for all nanowire arrays, whereas Mg content is found to increase relative to Zn, post annealing. In a similar study, Kim et al. described coating MgO nanowire surfaces with particle-like ZnO crystallites that sinter upon annealing, giving rise to increased dimensions,<sup>22</sup> and was further attributed to an increase in oxygen vacancies that allowed for the relaxation of interfacial strain.<sup>23</sup> In our work, we find that the ZnO lattice

consumes Mg<sup>2+</sup>, and nanowire dimensions decrease as the atomic exchange kinetics are reversed.

Presented in Figure 3a are the X-ray diffractograms of all annealed ZnMgO nanostructure arrays, along with the as-synthesized case (labeled as control). From the diffraction pattern of the as-synthesized nanowires, characteristic peaks associated with ZnO, Zn<sub>2</sub>SiO<sub>4</sub>, and MgO (JCPDS 05-0664, JCPDS 00-024-1469, and JCPDS 04-0849, respectively) can be observed (which indicates a slight degree of phase segregation between wurtzite ZnO and cubic MgO phases). Because the nanostructures retain hexagonal form, cubic MgO is not as predominant a reaction product as ZnO. Additionally, the formation of Zn<sub>2</sub>SiO<sub>4</sub> is largely confined to the substrate, as confirmed by EDX mapping. As shown in Figure 3b,c, annealing results in a right-shift of the ZnO *a* axis corresponding to the (100) plane ( $2\theta = 31.7^\circ$ ), as well as the ZnO *c* axis corresponding to the (002) plane ( $2\theta = 34.4^\circ$ ), by as high as  $\Delta 2\theta = 0.3^\circ$  in both cases (note: the presence of bimodal peaks arises from dissimilar *K* $\alpha$  excitation energies emitted from the diffractometer). Principally, the combined effect of a smaller electronegativity and electronic radius of Mg<sup>2+</sup> (Pauling electronegativity: 1.31 and 0.57 Å radius) to that of Zn<sup>2+</sup> (Pauling electronegativity: 1.65 and 0.60 Å radius) facilitates the formation of the Mg–O bond and leads to the decrease of observed lattice parameters.<sup>12,24–27</sup> Thus, Mg<sup>2+</sup> is effectively substituting Zn<sup>2+</sup> without significantly modifying the ZnO nanowire crystal structure, which further explains the reduced nanowire size distributions from Figure 2c. However, when these modified lattice parameters are scaled up to the average nanowire dimensions, we find that this phenomenon alone does not completely account for the observed reduction in array aspect ratio. Instead, reduced radial and axial

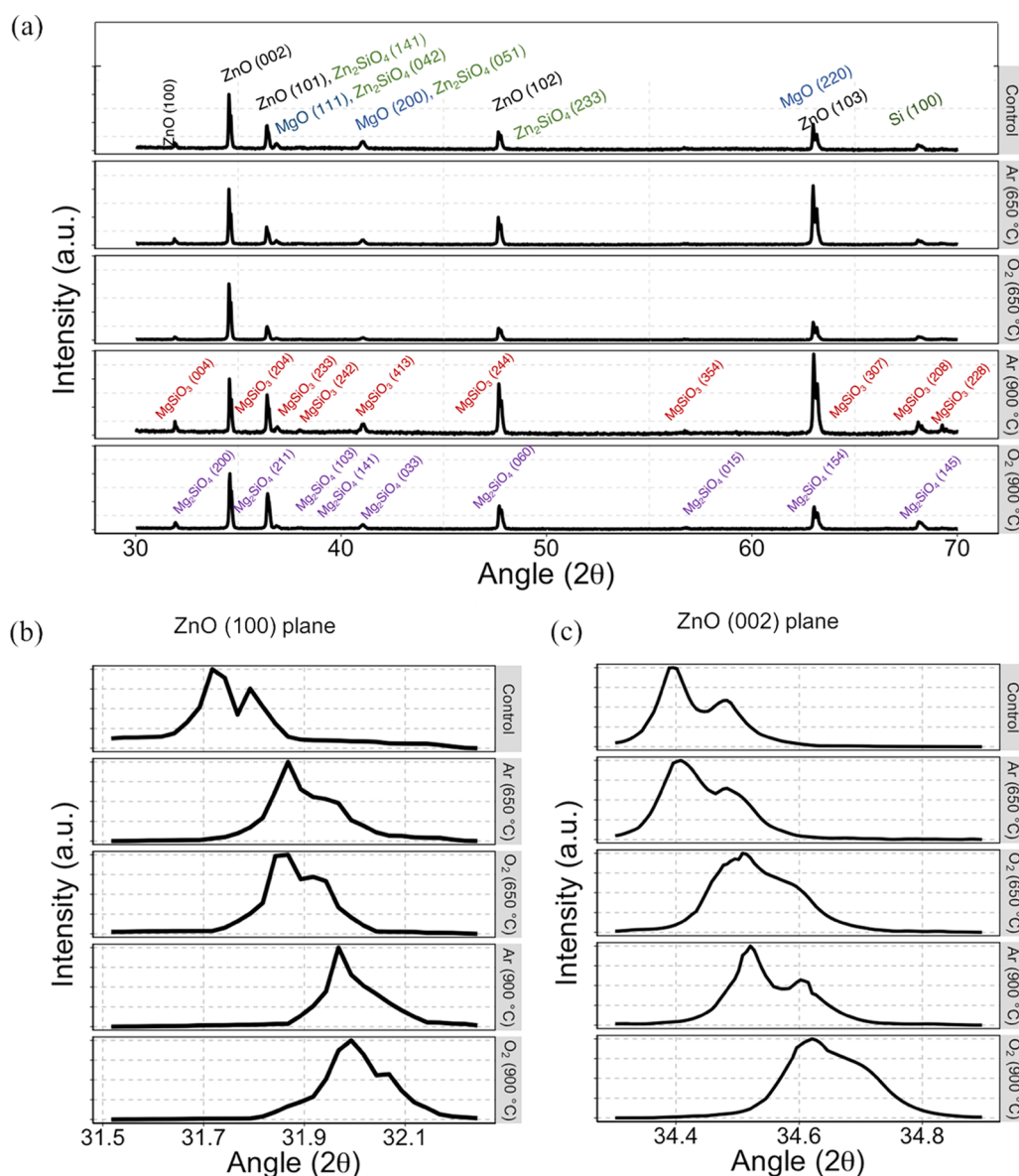


**Figure 3.** (a) Compiled XRD spectra of as-synthesized nanowires (labeled as control) and all nanowire anneal conditions. (b) Zoomed view of ZnO peaks emerging from the (100) plane and (c) ZnO (002) plane.

**Table 1. Lattice Parameter Modification of ZnMgO Wires as a Function of Annealing Condition**

anneal environment	anneal temperature (°C)	2θ peak (100) plane	2θ peak (002) plane	c (Å)	a (Å)
control	control	31.71708287	34.39533709	5.21	3.25
Ar	650	31.86748429	34.40787054	5.21	3.24
Ar	900	31.96775190	34.52067161	5.19	3.23
O <sub>2</sub>	650	31.86748429	34.50813816	5.19	3.24
O <sub>2</sub>	900	31.99281881	34.62093923	5.18	3.23

dimensions also stem from Zn<sup>2+</sup> dissociating completely from the nanowires, which is especially evident at high temperatures; and is supported by Zn deposits found along the sealed ampoule walls. Nonetheless, a summary of the 2θ peak shifts and lattice parameters is presented in Table 1. In addition to shifts of ZnO related peaks, new peaks emerge due to reactions on the substrate surface when annealed at high temperatures. Annealing in inert Ar results in the formation of MgSiO<sub>3</sub> (enstatite, JCPDS 01-088-1924), whereas annealing in reactive O<sub>2</sub> results in the formation of Mg<sub>2</sub>SiO<sub>4</sub> (forsterite, JCPDS 01-

079-1490). Notably, the diffraction pattern and luminescence spectra of these mineral forms are a strong function of crystal structure and imperfect stoichiometry, and these results are further discussed in the context of cathodoluminescence analysis.

The presence of Mg<sup>2+</sup> behaving as a substitutional ion in a fundamentally ZnO nanostructure is supported by the Raman spectrogram shown in Figure 4a. Increasing temperature shifts the peak position of the 1LO phonon mode from approximately 585 to 605 cm<sup>-1</sup>, as summarized in Figure 4b.

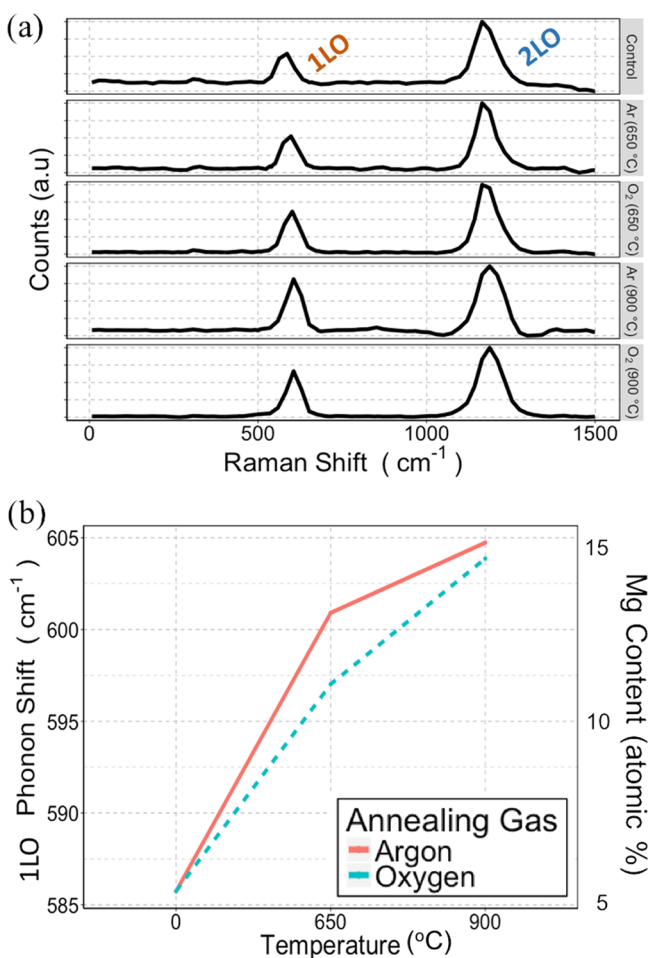


**Figure 4.** (a) Compiled Raman spectra of control group and all anneal conditions. (b) Extracted 1LO phonon shift extracted from Raman spectra as a function of temperature.

The modification of the 1LO peak position is found to be a greater function of temperature than that of the ambient gas environment, and is attributed to temperature-sensitive contributions from the LO mode of MgO<sup>28</sup> at 720 cm<sup>-1</sup>. Prior studies have reported that the maximal Mg content that the ZnO crystal can accommodate is 30%, corresponding to a Raman shift<sup>29</sup> of 615 cm<sup>-1</sup>. A model that maps Raman shift to Mg content was developed by Huso et al., utilizing fine control of Mg in sputtered ZnO thin films to explain a bowing feature in the Raman spectral response.<sup>29,30</sup> By cross-referencing the change in 1LO peak position to this model, as well as the modification of 2 $\theta$  peak diffractions of ZnO, the estimated Mg content incorporated is demonstrably increased via annealing and agrees with EDX analysis.

The cathodoluminescence (CL) spectra of all ZnMgO wires were measured both in the UV-A range, presented in Figure 5a.1, and in the UV-C range, presented in Figure 5b.1. Although the relative intensity of the band edge of ZnO ( $\approx$ 380 nm) dominates all other peaks across the spectrum, the intensity of the peak is found to decrease with increasing annealing temperature, given the same level of CL excitation current. This is attributed to the increased formation of O<sub>2</sub> defects along the wires, leading to an increased green-band emission (see Figure S.1, Supporting Information). The higher energy UV-C cathodoluminescence response, as presented in Figure 5b.1, was normalized to the peak at 156 nm,

corresponding to the bandgap of MgO. From the normalized response, the relative intensities of two other peaks can be compared, specifically those between 165 and 183 nm (linked to the band energy ranges of Mg<sub>2</sub>SiO<sub>4</sub> and MgSiO<sub>3</sub>)<sup>31,32</sup> and at 230 nm (linked to the band energy of Zn<sub>2</sub>SiO<sub>4</sub>).<sup>33,34</sup> The progressive attenuation of the Zn<sub>2</sub>SiO<sub>4</sub> peak intensity, shown in Figure 5b.3, and the increase of the Mg<sub>2</sub>SiO<sub>4</sub> and MgSiO<sub>3</sub> peak intensity, shown in Figure 5b.2, illustrate a relative exchange in composition, directly resulting from dissimilar anneal environments. Because molecules of Zn tend toward vapor pressures lower than that of Mg, ZnO nanostructures and Zn<sub>2</sub>SiO<sub>4</sub> will more preferably dissociate into Zn<sup>2+</sup>, O<sub>2</sub>, and SiO<sub>4</sub><sup>4-</sup> at higher anneal temperatures.<sup>21</sup> Isolated orthosilicate ions must therefore react to form forsterite molecules with Mg or equilibrate into silica if reaction-limited. As previously discussed, Zn deposits were found along the sealed ampoules, which indicate the vaporization and dissociation of Zn<sup>2+</sup> from the nanowire arrays. As O<sub>2</sub> is a reactive gas, Zn<sub>2</sub>SiO<sub>4</sub> is found to have completely converted into Mg<sub>2</sub>SiO<sub>4</sub>.<sup>31</sup> This is validated by the fact that the relative CL peaks associated with Mg<sub>2</sub>SiO<sub>4</sub> rise considerably under an oxidizing environment, until forming a close shoulder to the MgO band edge (in other words, exhibiting a distinct species, rather than coalescing with MgO). Annealing in Ar reduces the relative peak intensity of the Zn<sub>2</sub>SiO<sub>4</sub> peak to approximately 75% of its original level and in the inert environment, must only react with MgO in a kinetically limited manner to form half as much (molar ratio) of MgSiO<sub>3</sub><sup>32</sup> (see reactions of both anneal environments in Figure 1). Mishra et al. have described a modification of the orbital symmetries t<sub>1</sub> and t<sub>2</sub> of SiO<sub>4</sub><sup>4-</sup> ions, which have been influenced by the oxidizing reaction mechanics, contributing to a range of orthosilicate-ion peak position shifts found in Figure 5b.1. These results are illustrated in Figure 1 and summarize the complex reaction kinetics of Zn<sup>2+</sup> dissociation in conjunction with silicate formation as a function of the annealing environment.

Current–voltage measurements were conducted vertically across the nanowire arrays for the as-synthesized case, shown in Figure 6a, and for samples annealed at 900 °C in O<sub>2</sub>, shown in Figure 6b. Measurements were conducted in the dark and in the presence of UV-A (365 nm) and UV-C (254 nm) monochromatic illumination. The photoconductive properties of ZnO nanowires have long been attributed to the size effect of nanostructures, in correspondence with the adsorption/desorption of O<sub>2</sub> molecules along the nanowire surface, leading to surface band-bending and reducing channel resistivity.<sup>35–37</sup> The control case exhibited a negligible difference in conductance regardless of UV illumination wavelength, which suggests that band-to-band transition along the ZnO band edge largely contributes to its photoconductive behavior. However, in the annealed case, UV-A photoconduction is suppressed due to the increased formation of Zn vacancies, as evidenced by the attenuation of the peak ZnO band-edge luminescence, from Figure 5a.1. Specifically, the conductance was found to increase by almost 2 orders of magnitude (126 times) when illuminated with a UV-C source, as compared to a lower energy UV-A source, in which the annealed nanowire array only exhibited an increase of conduction by a factor of 11.

$$R_i = \frac{\Delta I}{PA} \quad (1)$$

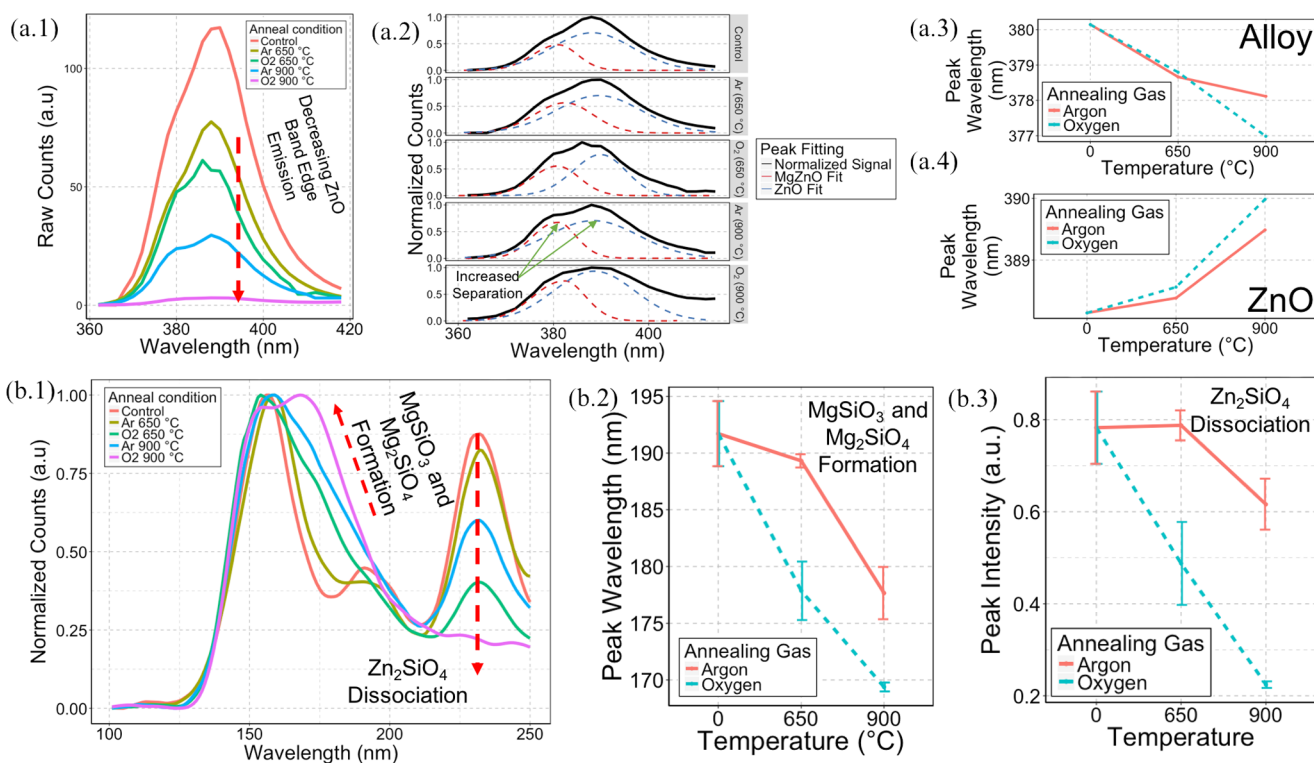


**Figure 5.** (a.1) Raw cathodoluminescence spectra at low-energy ultraviolet range (UV-A) near the ZnO band edge with (a.2) normalization of peak intensity and extracted peak intensities of (a.3) ZnMgO alloy and (a.4) ZnO. (b.1) Cathodoluminescence spectra at higher energy ultraviolet range (UV-C), highlighting (b.2) MgSiO<sub>3</sub> and Mg<sub>2</sub>SiO<sub>4</sub> formation from 170 to 190 nm peak shift and (b.3) Zn<sub>2</sub>SiO<sub>4</sub> dissociation at 230 nm with reduced peak intensity as a function of temperature and annealing gas environment.

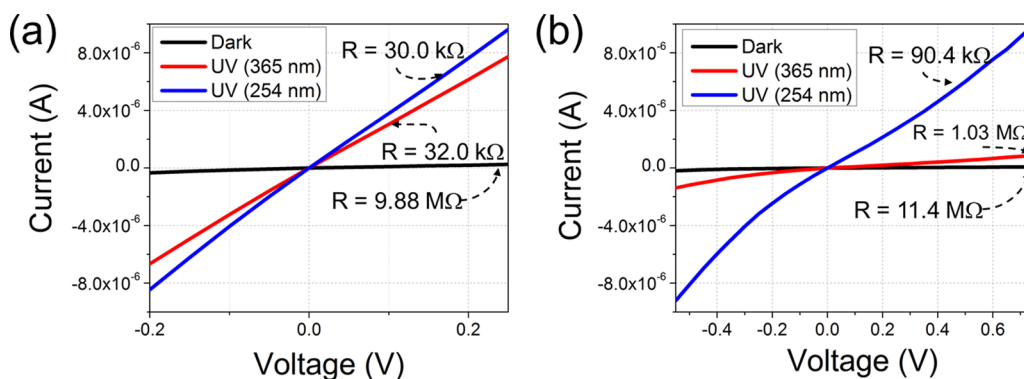


**Figure 6.** Current–voltage measurement of ZnMgO NW photodetector as a function of illumination conditions for nanowires that were (a) initially grown and (b) received thermal treatment at 900 °C in O<sub>2</sub>.

$$G = \left( \frac{\Delta I}{e} \right) / \left( \frac{P}{h\nu} \right) \quad (2)$$

The spectral responsivity ( $R_\lambda$ ) and photoconductive gain ( $G$ ) are key figures of merit that distinguish photodetector systems. These figures are defined by the relationships expressed in eqs 1 and 2, where  $\Delta I$  represents the difference between the photocurrent and dark current,  $P$  is the irradiation power,  $A$  is the area impinged by photons on the top surface of the nanostructures,  $h\nu$  is the illumination energy, and  $e$  is the elementary electronic charge.<sup>36</sup> The results of both performance characteristics are summarized in Table 2 for treated and untreated cases, compared between UV-A and UV-C illumination. In agreement with the observed changes in photoconduction, the most notable differences in  $R_\lambda$  and  $G$  occur for UV-A illumination ( $\lambda = 365$  nm), in which at least a

**Table 2.** Comparison of Photodetection Performance and Noise Metrics between As-Grown and Thermally Treated ZnMgO Nanowires as a Function of Ultraviolet Illumination Energy

photodetection metric	as-synthesized	annealed
$R_{\lambda=365}$ (A W <sup>-1</sup> )	$1.70 \times 10^{-5}$	$1.78 \times 10^{-4}$
$R_{\lambda=254}$ (A W <sup>-1</sup> )	$2.20 \times 10^{-4}$	$2.15 \times 10^{-4}$
$G_{\lambda=365}$	$5.79 \times 10^{-5}$	$9.85 \times 10^{-4}$
$G_{\lambda=254}$	$9.47 \times 10^{-4}$	$1.05 \times 10^{-3}$
$NEP_{\lambda=365}$ (W Hz <sup>-0.5</sup> )	$1.02 \times 10^{-8}$	$1.56 \times 10^{-9}$
$NEP_{\lambda=254}$ (W Hz <sup>-0.5</sup> )	$7.91 \times 10^{-10}$	$1.46 \times 10^{-9}$
$D^*_{\lambda=365}$ (cm Hz <sup>0.5</sup> W <sup>-1</sup> )	$3.10 \times 10^9$	$2.03 \times 10^{10}$
$D^*_{\lambda=254}$ (cm Hz <sup>0.5</sup> W <sup>-1</sup> )	$4.00 \times 10^{10}$	$2.17 \times 10^{10}$

single order of magnitude difference is estimated between the as-grown ( $R_{\lambda=365} = 1.70 \times 10^{-5} \text{ A W}^{-1}$ ,  $G_{\lambda=365} = 5.79 \times 10^{-5}$ ) and annealed cases ( $R_{\lambda=365} = 1.78 \times 10^{-4} \text{ A W}^{-1}$ ,  $G_{\lambda=365} = 9.85 \times 10^{-4}$ ), illustrating a suppression of UV-A photoconduction in the nanowire ensemble. Likewise, these figures do not change appreciably with UV-C illumination.

$$\text{NEP} = (1/R_{\lambda})(2qI_d + 4kT/R_v)^{1/2} \quad (3)$$

$$D^* = (Af)^{1/2}/\text{NEP} \quad (4)$$

To further investigate detection performance disparities, detector noise characteristics were calculated to distinguish the sensitivity of ZnMgO nanowires before and after thermal anneal. Noise equivalent power (NEP) and detectivity ( $D^*$ ) were evaluated according to eqs 3 and 4, where  $k$  is Boltzmann's constant,  $T$  is the absolute ambient temperature,  $I_d$  is the dark current for a specified operating voltages,  $R_v$  is the device differential resistance, and  $f$  is the amplifier bandwidth (taken as 1 kHz in this analysis).<sup>38</sup> Along with detector performance characteristics, detector noise metrics are also summarized in Table 2 and demonstrate a reduction of NEP for UV-A illumination (due to decreased spectral sensitivity), whereas a slight increase in NEP is observed for UV-C illumination. As highly sensitive detectors tend to exhibit low NEP and high  $D^*$ , the sensitivity of ZnMgO detectors increases in conjunction with suppressed photoconductive gain at  $\lambda = 365$  nm. Because annealing was found to reduce Zn content from the nanowire system, electrons from ZnO become less effective at band-to-band transitions, which diminishes the effect of surface band-bending from oxygen desorption.<sup>39</sup> On the substrate surface, the formation of  $\text{Mg}_2\text{SiO}_4$  results in stoichiometrically heterogeneous MgO films, thereby increasing thermal noise. Annealing in oxygen was shown to increase the incidence of  $\text{O}_2$  related green-band defects (see Figure S.1, Supporting Information), which contribute directly to thermal agitation of charge carriers.<sup>40–42</sup> However, this NEP increase is negligible in comparison to the modification of spectral sensitivity under UV-A illumination, which suggests a minor design tradeoff between noise and tunability.

### 3. CONCLUSIONS

In conclusion, high-quality ZnMgO nanowires have been synthesized utilizing a novel growth mechanism that incorporates Mg dissociated from  $\text{Mg}_3\text{N}_2$ , in tandem with the carbothermal reduction of ZnO. Modification of the size characteristics, crystal lattice properties, and spectral response from annealing were found to be internally consistent with measured Mg content. In particular, EDX, Raman, and CL revealed a spectral evolution for each treatment group of nanowire arrays, giving rise to increased  $\text{Mg}^{2+}$  incorporation, along with the dissociation of  $\text{Zn}^{2+}$ . Statistical inference (ANOVA paired with Tukey's range test) was undertaken to discern a reduction of nanowire dimensions, and was cross-referenced to a modification of the ZnO lattice parameters, as well as the formation of Zn vacancies.

Suppressed photoconductivity under UV-A illumination with retained photoconductivity under high-energy UV-C illumination was observed for samples post thermal treatment. An order of magnitude difference for both spectral responsivity and photoconductive gain between the annealed and control cases confirms the tunable filtering of high-energy ultraviolet spectral responsivity. Increased thermal noise from the high-temper-

ature  $\text{O}_2$  anneal process was associated with the increase of oxygen-related defects contributing to thermal agitation, which may present a design tradeoff in integrating ZnMgO as solar-blind detectors. Thus, these results indicate that synthesized ZnMgO nanowires demonstrate promising selective UV-C detection capabilities, in which controlled postsynthesis thermal treatment may effectively tune for selective, high-pass, solar-blind ultraviolet detection.

### 4. EXPERIMENTAL DETAILS

ZnMgO nanowires were synthesized using a vapor-phase transport method comprised of a carbothermal reduction of ZnO in tandem with the dissociation of  $\text{Mg}_3\text{N}_2$  as the source of Mg. In a single zone reaction tube furnace, a ceramic boat containing a 1:1 molar ratio mixture of ZnO and graphite powder (total 3 g) was placed upstream to another ceramic boat containing 10 g of  $\text{Mg}_3\text{N}_2$  powder. Silicon (100) substrates were cleaned in piranha solution (70%  $\text{H}_2\text{SO}_4$ , 30%  $\text{H}_2\text{O}_2$ ) and were treated using a buffered oxide etchant (2% hydrofluoric acid). Subsequently, a thin 10 nm ZnO film was sputtered (Lesker PVD 250) atop substrates to form a catalyst seed. The samples were then cleaned using acetone, isopropyl alcohol, and water before being positioned downstream relative to the source materials. The tube furnace was evacuated and brought to 500 °C. Upon reaching the target temperature, Ar was introduced to the system at a flow rate of 87.4 sccm, while maintaining a steady state pressure of 150 Torr throughout the process. At a rate of 500 °C  $\text{h}^{-1}$ , the furnace temperature continued increasing up to 1100 °C, upon which the temperature was held for 24 min. In the final 10 min of this growth period,  $\text{O}_2$  was introduced to the system at a flow rate of 7.5 sccm. Finally, the system was allowed to cool naturally, without gas flow, under vacuum. This process produced a conformal, coarse, light-gray deposition consisting of nanowire and submicron columnar growth on the substrate surface. The sample was then cleaved into five equally sized pieces, four of which were sealed in separate quartz ampoules of Ar and  $\text{O}_2$  environments. The sealed samples underwent a unique combination of thermal annealing (650 and 900 °C), with a fixed anneal time of 30 min (conditions summarized in Table 1). In all cases, a reflective metallic reduced Zn deposit (confirmed with EDX) was found to have condensed along the ampoule walls. The four samples, along with the unannealed "control" case, were morphologically characterized with a field emission scanning electron microscope (FESEM, Hitachi S4700-II, excitation 15 kV). A postgrowth analysis of nanowire size distributions was conducted by tracing radial and axial dimensions of a sample size of approximately  $n = 1000$  nanowires, for each treatment group, along nine equally spaced sample regions (corners, edges, and center) within ImageJ (image processing) software. The relative Mg content was determined using an energy-dispersive X-ray (EDX) spectroscopy attachment by sampling the aforementioned regions along each sample surface, at an excitation energy of 15 kV. Modification of crystal structures was determined with a high-resolution X-ray diffractometer (PANalytical XPert PRO XRD,  $K\alpha_1 = 1.540598 \text{ \AA}$ ,  $K\alpha_2 = 1.544426 \text{ \AA}$ ). Ultraviolet luminescence spectra were ascertained using a JEOL JSM 630 SEM with an attached cathodoluminescence (CL) system, operating at an excitation current of 0.5 nA for UV-A analysis and 2 nA for UV-C analysis. Raman spectra were gathered with a Renishaw InVia spectroscopy system with a 100× objective lens, using a laser source of  $\lambda = 488$  nm. Finally, conductance

modification subject to UV illumination (UVP EL Series Lamp, 45 mW cm<sup>-2</sup>) were determined with a Keithley 4200 Semiconductor Analyzer System within a “light-tight” micro-manipulator probe station, utilizing tungsten-tipped soft probes. Postexperimental processing of data which included cleaning, analysis, and visualization was performed in R language with the ggplot2 library.

## ■ ASSOCIATED CONTENT

### ■ Supporting Information

The Supporting Information is available free of charge on the ACS Publications website at DOI: 10.1021/acsomega.7b01362.

ANOVA tables and results of Tukey pairwise analysis comparison of anneal groups exhibited in Table S1 for length and Table S2 for diameter; green-band emission from high-temperature O<sub>2</sub> anneal shown in Figure S1 (PDF)

## ■ AUTHOR INFORMATION

### Corresponding Authors

\*E-mail: eazhar@asu.edu (E.A.A.).

\*E-mail: hongbin.yu@asu.edu (H.Y.).

### ORCID

Ebraheem Ali Azhar: 0000-0002-3461-6474

### Notes

The authors declare no competing financial interest.

## ■ ACKNOWLEDGMENTS

This project was financially supported by NASA NNX-15CG10C through a subcontract from Structured Materials Industries, Inc., Piscataway, New Jersey 08854, United States. The authors gratefully acknowledge the assistance of David Wright of the LeRoy Eyring Center for Solid State Science (CSSS) for use of their single zone growth and anneal tube furnaces, as well as their high-resolution X-ray diffraction facilities. For the use of electron microscopy facilities, the authors gratefully acknowledge the Center for Solid State Electronics Research (CSSER) at Arizona State University. The authors also acknowledge Hanxiao Liu and Dr. Fernando Ponce for their assistance with cathodoluminescence data collection and analysis, as well as Dr. Sefaattin Tongay and Bin Chen for the use of their Raman facilities.

## ■ REFERENCES

- (1) Chen, G.; Abou-Galala, F.; Xu, Z.; Sadler, B. M. Experimental Evaluation of LED-Based Solar Blind NLOS Communication Links. *Opt. Express* **2008**, *16*, 15059–15068.
- (2) El-Shimy, M. A.; Hranilovic, S. Binary-Input Non-Line-of-Sight Solar-Blind UV Channels: Modeling, Capacity and Coding. *J. Opt. Commun. Networking* **2012**, *4*, 1008–1017.
- (3) Yang, J.; Li, X. Y.; Zhao, F.; Chen, X. Y.; Shao, P. An Algorithm of Channel Sharing for the Solar Blind NLOS Ultraviolet Ad-Hoc Network Based on the Hybrid Genetic Algorithm. *Appl. Mech. Mater.* **2014**, *543–547*, 2850–2853.
- (4) Li, T.; Lambert, D. J. H.; Wong, M. W.; Collins, C. J.; Yang, B.; Beck, A. L.; Chowdhury, U.; Durpui, R. D.; Campbell, J. C. Low-Noise Back-Illuminated Al<sub>x</sub>Ga<sub>1-x</sub>N-Based p-i-n Solar-Blind Ultraviolet Photodetectors. *IEEE J. Quantum Electron.* **2001**, *37*, 538–545.
- (5) Collins, C. J.; Chowdhury, U.; Wong, M. M.; Yang, B.; Beck, A. L.; Dupuis, R. D.; Campbell, J. C. Improved Solar-Blind Detectivity Using an Al<sub>x</sub>Ga<sub>1-x</sub>N Heterojunction p-i-n Photodiode. *Appl. Phys. Lett.* **2002**, *80*, 3754–3756.
- (6) Cui, W.; Guo, D.; Zhao, X.; Wu, Z.; Li, P.; Li, L.; Cui, C.; Tang, W. Solar-Blind Photodetector Based on Ga<sub>2</sub>O<sub>3</sub> Nanowires Array Film Growth from Inserted Al<sub>2</sub>O<sub>3</sub> Ultrathin Interlayers for Improving Responsivity. *RSC Adv.* **2016**, *6*, 100683–100689.
- (7) Tang, H.; Kwon, B. J.; Park, J.-Y. Characterizations of Individual ZnMgO Nanowires Synthesized by a Vapor-Transport Method. *Phys. Status Solidi A* **2010**, *207*, 2478–2482.
- (8) Liu, W.; Liang, Y.; Xu, H.; Wang, L.; Zhang, X.; Liu, Y.; Hark, S. Heteroepitaxial Growth and Spatially Resolved Cathodoluminescence of ZnO/MgZnO Coaxial Nanorod Arrays. *J. Phys. Chem. C* **2010**, *114*, 16148–16152.
- (9) Lange, M.; Dietrich, C. P.; Zúñiga-Pérez, J.; et al. MgZnO/ZnO Quantum Well Nanowire Heterostructures with Large Confinement Energies. *J. Vac. Sci. Technol., A* **2011**, *29*, No. 03A104.
- (10) Vanjaria, J. V.; Azhar, E. A.; Yu, H. Broad Range Tuning of Structural and Optical Properties of Zn<sub>x</sub>Mg<sub>1-x</sub>O Nanostructures Grown by Vapor Transport Method. *J. Phys. D: Appl. Phys.* **2016**, *49*, No. 465103.
- (11) Hwang, D.-K.; Jeong, M.-C.; Myoung, J.-M. Effects of Deposition Temperature on the Properties of Zn<sub>1-x</sub>Mg<sub>x</sub>O Thin Films. *Appl. Surf. Sci.* **2004**, *225*, 217–222.
- (12) Liu, W.; Gu, S.; Zhu, S.; Ye, J.; Qin, F.; Liu, S.; Zhou, X.; Hu, L.; Zhang, R.; Shi, Y.; Zheng, Y. The Deposition and Annealing Study of MOCVD ZnMgO. *J. Cryst. Growth* **2005**, *277*, 416–421.
- (13) Huso, J.; Morrison, J. L.; Hoeck, H.; Casey, E.; Bergman, L.; Pounds, T. D.; Norton, M. G. Low Temperature LO-Phonon Dynamics of MgZnO Nanoalloys. *Appl. Phys. Lett.* **2007**, *91*, No. 111906.
- (14) Pietrzyk, M. A.; Stachowicz, M.; Wierzbicka, A.; Dłuzewski, P.; Jarosz, D.; Przewdzicka, E.; Kozanecki, A. Growth Conditions and Structural Properties of ZnMgO Nanocolumns on Si(111). *J. Cryst. Growth* **2014**, *408*, 102–106.
- (15) Kim, D. C.; Lee, J. H.; Mohanta, S. K.; Cho, H. K.; Kim, H.; Lee, J. Y. Density and Aspect Ratio Controlled MgZnO Nanowire Arrays by Spontaneous Phase Separation Effect. *CrystEngComm* **2011**, *13*, 813–818.
- (16) Thierry, R.; Perillat-Merceroz, G.; Jouneau, P. H.; Ferret, P.; Feuillet, G. Core-shell Multi-Quantum wells in ZnO/ZnMgO Nanowires with High Optical Efficiency at Room Temperature. *Nanotechnology* **2012**, *23*, No. 085705.
- (17) Polyakov, A. Y.; Smirnov, N. B.; Govorkov, A. V.; Kozhukhova, E. A.; Belogorokhov, A. I.; Norton, D. P.; Kim, H. S.; Pearton, S. J. Shallow and Deep Centers in as-Grown and Annealed MgZnO/ZnO Structures with Quantum Wells. *J. Electron. Mater.* **2010**, *39*, 601–607.
- (18) Shimpi, P.; Gao, P.-X.; Goberman, D. G.; Ding, Y. Low Temperature Synthesis and Characterization of MgO/ZnO Composite Nanowire Arrays. *Nanotechnology* **2009**, *20*, No. 125608.
- (19) Kar, J. P.; Jeong, M. C.; Lee, W. K.; Myoung, J. M. Fabrication and Characterization of Vertically Aligned ZnMgO/ZnO Nanowire Arrays. *Mater. Sci. Eng., B* **2008**, *147*, 74–78.
- (20) Zhou, W. W.; Sun, L.; Yu, T.; Zhang, J. X.; Gong, H.; Fan, H. J. The Morphology of Au@MgO Nanopeapods. *Nanotechnology* **2009**, *20*, No. 455603.
- (21) Lamoreaux, R. H.; Hildenbrand, D. L.; Brewer, L. High-Temperature Vaporization Behavior of Oxides II. Oxides of Be, Mg, Ca, Sr, Ba, B, Al, Ga, In, Tl, Si, Ge, Sn, Pb, Zn, Cd, and Hg. *J. Phys. Chem. Ref. Data* **1987**, *16*, 419–443.
- (22) Kim, H. W.; Shim, S. H.; Lee, C. Effects of Thermal Annealing on the Properties of ZnO-Coated MgO Nanowires. *Mater. Sci. Eng., B* **2007**, *136*, 148–153.
- (23) Shimpi, P.; Ding, Y.; Suarez, E.; Ayers, J.; Gao, P.-X. Annealing Induced Nanostructure and Photoluminescence Property Evolution in Solution-Processed Mg-Alloyed ZnO Nanowires. *Appl. Phys. Lett.* **2010**, *97*, No. 103104.
- (24) Singh, A.; Kumar, D.; Khanna, P. K.; Kumar, A.; Kumar, M.; Kumar, M. Anomalous Behavior in ZnMgO Thin Films Deposited by sol-gel Method. *Thin Solid Films* **2011**, *519*, 5826–5830.

- (25) Wei, X. Q.; Zhao, R. R.; Wang, Y. J.; Liu, L. Y.; Cao, B. Q. Annealing Effects in Non-Polar ZnMgO Thin Films Fabricated by PLD. *Surf. Eng.* **2012**, *28*, 678–682.
- (26) Das, A. K.; Misra, P.; Ajimsha, R. S.; Bose, A.; Joshi, S. C.; Porwal, S.; Sharma, T. K.; Oak, S. M.; Kukreja, L. M. Effect of Mg Diffusion on Photoluminescence Spectra of MgZnO/ZnO Bi-Layers Annealed at Different Temperatures. *J. Appl. Phys.* **2013**, *114*, No. 183103.
- (27) Saha, S.; Pandey, S. K.; Nagar, S.; Chakrabarti, S. Effect of Annealing Temperature on Optical and Electrical Properties of Nitrogen Implanted p-Type ZnMgO Thin Films. *J. Mater. Sci.: Mater. Electron.* **2015**, *26*, 9759–9765.
- (28) Huso, J.; Che, H.; Thapa, D.; Morrison, J. L.; Norton, M. G.; Bergman, L. Phonon dynamics and anharmonicity in phase segregated structural domains of MgZnO film. *Appl. Phys. Lett.* **2014**, *104*, No. 031908.
- (29) Huso, J.; Che, H.; Thapa, D.; Canul, A.; McCluskey, M. D.; Bergman, L. Phonon Dynamics and Urbach Energy Studies of MgZnO Alloys. *J. Appl. Phys.* **2015**, *117*, No. 125702.
- (30) Ye, J. D.; Teoh, K. W.; Sun, X. W.; Lo, G. Q.; Kwong, D. L.; Zhao, H.; Gu, S. L.; Zhang, R.; Zheng, Y. D.; Oh, S. A.; Zhang, X. H.; Tripathy, S. Effects of Alloying and Localized Electronic States on the Resonant Raman Spectra of Zn<sub>1-x</sub>Mg<sub>x</sub>O Nanocrystals. *Appl. Phys. Lett.* **2007**, *91*, No. 091901.
- (31) Shankland, T. J. Band Gap of Forsterite. *Science* **1968**, *161*, 51–53.
- (32) Stashans, A.; Eras, L.; Chamba, G. Modelling of Al Impurity in Perovskite and Ilmenite Structures of MgSiO<sub>3</sub>. *Phys. Chem. Miner.* **2010**, *37*, 191–199.
- (33) Mishra, K. C.; Johnson, K. H.; DeBoer, B. G.; Berkowitz, J. K.; Olsen, J.; Dale, E. A. First Principles Investigation of Electronic Structure and Associated Properties of Zinc Orthosilicate Phosphors. *J. Lumin.* **1991**, *47*, 197–206.
- (34) Karazhanov, S. Z.; Ravindran, P.; Fjellvåg, H.; Svensson, B. G. Electronic Structure and Optical Properties of ZnSiO<sub>3</sub> and Zn<sub>2</sub>SiO<sub>4</sub>. *J. Appl. Phys.* **2009**, *106*, No. 123701.
- (35) Soci, C.; Zhang, A.; Xiang, B.; Dayeh, S. A.; Aplin, D. P. R.; Park, J.; Bao, X. Y.; Lo, Y. H.; Wang, D. ZnO Nanowire UV Photodetectors with High Internal Gain. *Nano Lett.* **2007**, *7*, 1003–1009.
- (36) Yu, H.; Azhar, E. A.; Belagodu, T.; Lim, S.; Dey, S. ZnO Nanowire Based Visible-Transparent Ultraviolet Detectors on Polymer Substrates. *J. Appl. Phys.* **2012**, *111*, No. 102806.
- (37) Xie, X.; Zhang, Z.; Li, B.; Wang, S.; Jiang, M.; Shan, C.; Zhao, D.; Chen, H.; Shen, D. Enhanced Solar-Blind Responsivity of Photodetectors Based on Cubic MgZnO Films via Gallium Doping. *Opt. Express* **2014**, *22*, 246.
- (38) Sze, S. M.; Ng, K. K. *Physics of Semiconductor Devices*, 3rd ed.; Wiley-Interscience: Hoboken, NJ, 2006; p 39840.
- (39) Feng, Z. C. *Handbook of Zinc Oxide and Related Materials: Volume Two, Devices and Nano-Engineering*; CRC Press, 2012; Vol. 2.
- (40) Hsu, N. E.; Hung, W. K.; Chen, Y. F. Origin of defect emission identified by polarized luminescence from aligned ZnO nanorods. *J. Appl. Phys.* **2004**, *96*, 4671–4673.
- (41) Djurišić, A. B.; Leung, Y. H.; Tam, K. H.; Hsu, Y. F.; Ding, L.; Ge, W. K.; Zhong, Y. C.; Wong, K. S.; Chan, W. K.; Tam, H. L.; Cheah, K. W.; Kwok, W. M.; Phillips, D. L. Defect emissions in ZnO nanostructures. *Nanotechnology* **2007**, *18*, No. 095702.
- (42) Lee, C.-T.; Lin, T.-S.; Chen, C.-H. ZnO-Based Solar Blind Ultraviolet-B Photodetectors Using MgZnO Absorption Layer. *J. Electron. Mater.* **2015**, *44*, 4722–4725.